J. Fluid Mech. (2013), *vol.* 730, *pp.* 607–625. © Cambridge University Press 2013
doi:10.1017/jfm.2013.354

The viscous Savart sheet

E. Villermaux[1],†, V. Pistre[2] and H. Lhuissier[1]

[1]Aix Marseille Université, CNRS, Centrale Marseille, IRPHE UMR 7342, F-13384, Marseille, France
[2]TECHNI-PROCESS, ZI La Muscatelle, 13790 Châteauneuf-Le-Rouge, France

(Received 7 March 2013; revised 12 June 2013; accepted 5 July 2013;
first published online 2 August 2013)

We study the viscous version of the planar Savart sheet problem, using an impacting liquid jet up to 300 times more viscous than water. Two surprising observations are made, contrasting with the traditional case introduced by Savart where viscosity plays no role. First, if the radius of a viscous sheet is typically reduced compared to the case of water for a given jet radius and impacting velocity, the smooth–flapping transition is delayed, allowing for smooth sheet radii substantially bigger than those permitted with water at large impacting Weber number. Second, the drop size distribution is bimodal, with a substantial fraction of the drops having a very small, well-defined diameter. We understand these two facts in terms of an additional model experiment, and simple physical arguments.

Key words: aerosols/atomization, breakup/coalescence, drops and bubbles

1. Introduction

In addressing the nature of liquid cohesion, Félix Savart proposed studying the shape of deviated liquid streams. The principle consists in letting a liquid jet impact normally a flat solid disk (Savart 1833*a*,*b*). The mass and momentum of the incident jet are radially distributed in a symmetrical fashion, forming a stationary expanding sheet; the expansion is bounded at some radial location, and the liquid focuses into ligaments, further breaking into stable drops (figure 1). This simple configuration has allowed us to discover a wealth of phenomena characteristic of atomization processes, whether of industrial (Lefebvre 1989) or natural origin (Eggers & Villermaux 2008). It has been established how liquid surface tension limits the maximal radial extension of the sheet when it is smooth (Taylor 1959*a*,*b*), and the role of the ambient medium on the existence of a flapping sheet regime (Squire 1953; Huang 1970; Villermaux & Clanet 2002; Bremond, Clanet & Villermaux 2007; Lhuissier & Villermaux 2009) has been documented and understood, including the reason for the formation of sharp folds at the sheet's extremity in that case (Lhuissier & Villermaux 2012). The drop formation process has been the subject of more recent investigations in both the smooth and flapping regimes, essentially through the measurement of mean drop sizes (Clanet & Villermaux 2002; Villermaux & Clanet 2002; Bremond *et al.* 2007), but also with more detailed insights into the construction of the complete drop size distribution (Bremond & Villermaux 2006).

---

† Also at: Institut Universitaire de France. Email address for correspondence: villermaux@irphe.univ-mrs.fr

https://doi.org/10.1017/jfm.2013.354 Published online by Cambridge University Press

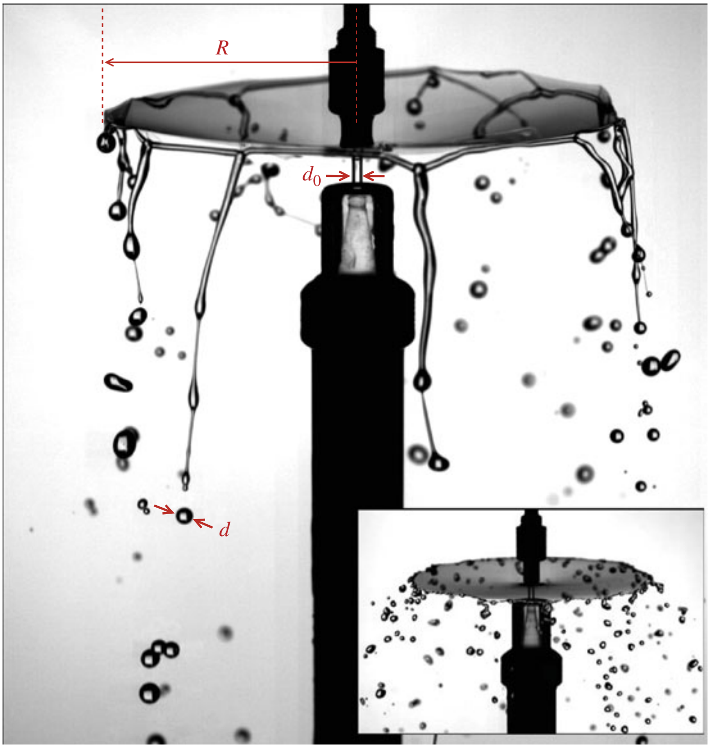

FIGURE 1. (Colour online) An instantaneous view of the sheet with a viscous fluid ($\eta = 320\times10^{-3}$ Pa s), illustrating the experimental setup and the relevant quantities of interest: $d_0 = 3$ mm. The inset shows water with the same injection parameters, for reference.

However, all of the above-mentioned studies were done with low-viscosity liquids (water, ethanol), and indeed viscosity did not matter in these cases. Furthermore, Savart (1833*a*) mentions that he had occasionally used 'gummed' water, probably meaning that a mixture of 'gum arabic' and water had been used as a working liquid (but with no indication of the viscosity of the resulting liquid) causing, according to Savart, no qualitative difference from the pure water case.

Viscous liquid sheets are, nevertheless, commonplace in various situations ranging from the fabrication of glass to the dynamics of tephra bubbles in volcanic explosions (Mastin 2007), or the dynamics of the Earth's crust, among others: see Howell, Scheid & Stone (2010) and references therein. Their breakup into drops is of prime importance in the food, cosmetics and cement industries for making various prills and granules, and this is usually achieved using standard hollow cone atomizers (Lefebvre 1989; Yule & Dunkey 1994), which produce an expanding conical liquid sheet breaking up at some point. Thus, extending Savart's observations to the case where liquid viscosity matters has, besides its academic interest, well-motivated applications.

We intend here to describe both the sheet shape (maximal radius, smooth–flapping transition) and the atomization characteristics (drop size distribution) of the planar Savart sheet, using an impacting liquid jet up to 300 times more viscous than water, made of a solution of maltodextrin with water (§ 2). In contrast with the traditional case introduced by Savart, where viscosity plays no role, two salient observations are made. First, for a given jet radius and impacting velocity, the viscous sheet radius

https://doi.org/10.1017/jfm.2013.354 Published online by Cambridge University Press

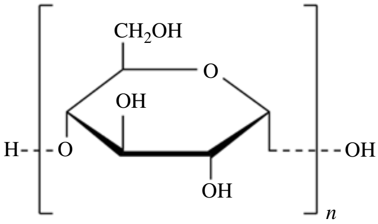

FIGURE 2. The D-glucose unit in the maltodextrin molecule.

can be larger compared to the case of water because the smooth–flapping transition is delayed as the jet velocity is increased (§ 3). Then, the final drop size distribution is bimodal, with a substantial fraction of the drops having a smaller, well-defined diameter (§ 4). These two original facts can be understood by simple arguments and by resorting to an additional model experiment (§ 5), featuring the ingredients to reproduce and understand the bimodality.

2. Working fluid, setup and parameters

We have been using dilutions of maltodextrin, a powder easily incorporated into water, as our working fluid. Maltodextrin is a polysaccharide that is used as a food additive. It is produced from starch by partial hydrolysis and is usually found as a white hygroscopic spray-dried powder, available in large quantities and commonly used for the production of sodas and candy. Maltodextrin consists of D-glucose units connected in chains of variable length (figure 2) and is typically composed of a mixture of chains that vary from three to seventeen glucose units in length. When diluted in water it is a Newtonian liquid, with a viscosity of η proportional to its polymerization index (Dokic, Jakovljevic & Dokic-Baucal 1998), and strongly dependent on its concentration: a mixture of 46 g per 100 g of solution has a viscosity of $\eta = 60 \times 10^{-3}$ Pa s while 56 g per 100 g of solution gives a viscosity of $\eta = 320 \times 10^{-3}$ Pa s. The surface tension of the mixtures is about $\sigma = 67 \times 10^{-3}$ N m^{-1} (Semenova *et al.* 2003). The density ρ is about 1200 kg m^{-3} for the concentrations we have been using.

Once diluted at the desired viscosity, the solution is sealed in a closed container and pushed under pressure through an injector with a contracted nozzle to produce a potential jet of radius $r_0 = d_0/2 = 1.5$ mm. We let the jet impact on a smooth circular impactor of radius $r_i = 3$ mm, varying the jet velocity u_0, typically in the range 1–10 m s^{-1}. The sheet is forced to exit the impact surface parallel to it (horizontally) by means of a thin copper jacket, as described in Clanet & Villermaux (2002). Thus formed, the sheet is imaged quantitatively to measure its radius R and the drop sizes d in the resulting spray, as seen in figure 1.

There are several dimensionless parameters in this problem, each associated with distinct facets of the phenomenon. The Weber number, comparing liquid inertia ρu_0^2 with capillary confinement σ / r_0,

$$We = \frac{\rho u_0^2 r_0}{\sigma}, \tag{2.1}$$

spans between 100 and 3000, indicating that the jet is momentum-dominated, hence the formation of an extended sheet.

https://doi.org/10.1017/jfm.2013.354 Published online by Cambridge University Press

The Reynolds number, comparing the transit time r_0/u_0 with the diffusion time r_0^2/ν, where $\nu = \eta/\rho$,

$$Re = \frac{u_0 r_0}{\nu}, \tag{2.2}$$

is relevant to evaluation of viscous dissipation at the impact location. It varies from 30 for the lowest velocity with the most viscous mixture ($\eta = 320 \times 10^{-3}$ Pa s), to 5×10^4 with pure water ($\eta = 10^{-3}$ Pa s). The Ohnesorge number $Oh = \sqrt{We}/Re$, a combination of the two independent numbers above, is the ratio of the viscous capillary time $\eta r_0/\sigma$ to the inertial capillary time $\sqrt{\rho r_0^3/\sigma}$, and indicates the nature of ligament destabilization, leading to drops. It is much smaller than unity with water, and of order unity with the most viscous mixture at $\eta = 320 \times 10^{-3}$ Pa s.

Finally, it will be seen that gravity is responsible for the detachment of the drops at the edge of the sheet, involving a gravitational capillary (equivalently, Ohnesorge) number

$$Ca = \frac{\eta\sqrt{ga}}{\sigma}, \tag{2.3}$$

where $a = \sqrt{2\sigma/\rho g}$ is the capillary length scale, of order unity for the most viscous solution. Gravity, on the other hand, does not influence the injection conditions, as the Froude number

$$Fr = \frac{u_0^2}{g d_0} \tag{2.4}$$

is much larger than unity. The orientation of the jet, which is upwards in figure 1 to facilitate the evacuation of residual bubbles in the feeding circuit at the beginning of the experiments, could equally have been downwards, with no consequences.

3. Sheet shape

3.1. *Localization of viscous dissipation*

For an axisymmetric liquid sheet with thickness $h(r)$, sustaining a steady radial motion with velocity $u(r)$, momentum and mass balances yield

$$\rho h r u \partial_r u = \partial_r (r h \sigma_{rr}) - h\sigma_{\theta\theta}, \tag{3.1}$$

$$\partial_r (h r u) = 0 \tag{3.2}$$

where the stresses (Landau & Lifshitz 1987), in the Trouton approximation (see Howell *et al.* 2010 for a derivation in that precise context), are given by

$$\sigma_{rr} = 2\eta(2\partial_r u + u/r), \tag{3.3}$$

$$\sigma_{\theta\theta} = 2\eta(\partial_r u + 2u/r). \tag{3.4}$$

Evaluating the relative importance of viscosity amounts to comparing the magnitude $\rho h u^2/r$ of the inertial term in (3.1) with that of the viscous term $\eta h u/r$, namely to determine the radial distance r beyond which inertia dominates over viscous dissipation, that is to say

$$\frac{ur}{\nu} > 1. \tag{3.5}$$

For typical impacting velocities u_0 of order 1 m s^{-1}, and even for a liquid 300 times more viscous than water, it is clear that the fluid particles in the sheet undergo a

https://doi.org/10.1017/jfm.2013.354 Published online by Cambridge University Press

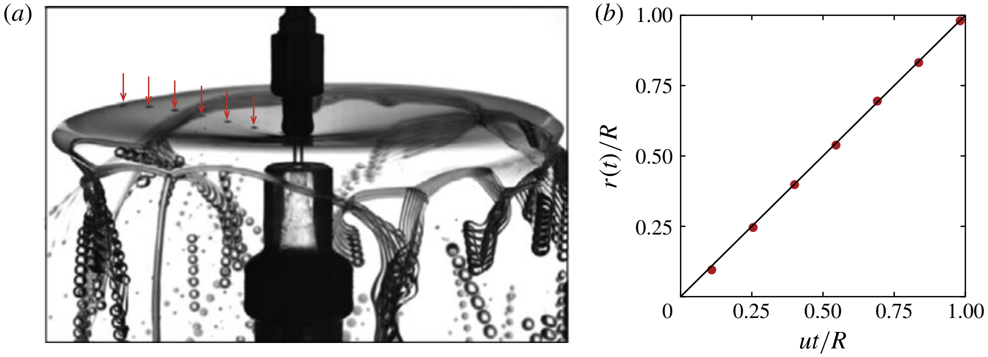

FIGURE 3. (Colour online) (*a*) Superposition of seven consecutive images equally spaced in time by 4/1000 s showing the ballistic motion of a bubble injected in the sheet. The successive positions of the bubble are indicated by an arrow. (*b*) The corresponding trajectory: $\eta = 320 \times 10^{-3}$ Pa s, $u_0 = 4.55$ m s^{-1}, $u = 3.38$ m s^{-1}, $R = 8.5$ cm.

ballistic radial motion (constant velocity $\partial_r u = 0$) once they have left the impactor ($r_i = 3$ mm). Figure 3 demonstrates that a bubble, injected by chance in the jet, does indeed undergo a ballistic motion towards the sheet edge.

Viscous resistance therefore does not take place in the sheet itself, but must be concentrated in the boundary layer developing on the solid impactor. The thickness (or *displacement thickness*, owing to the use we will make of it further: Schlichting 1987) of that boundary layer is of order

$$\delta = \sqrt{\frac{\nu r_i}{u_0}}. \tag{3.6}$$

If δ is small compared to the radius of the impactor r_i and even more compared to the radial extent of the sheet (see (3.5)), it may compare with the sheet thickness itself. Its inviscid value at the impactor lip is given by mass conservation,

$$h_{inv} = \frac{r_0^2}{2r_i} = 0.375\,\text{mm}, \tag{3.7}$$

and, given the typical value of the Reynolds number Re, it is clear that the ratio

$$\beta = \frac{\delta}{h_{inv}} = 2\sqrt{\frac{(r_i/r_0)^3}{Re}} \tag{3.8}$$

may reach values of order unity in the present case. Therefore, a non-negligible fraction of the incident momentum flux $\rho\pi r_0^2 u_0^2$ is lost at impact by viscous friction, whereas, as discussed previously, viscosity does not affect the sheet development once it has left the impactor. We detail below the consequences of this loss on the sheet's features.

3.2. *Smooth sheet*

At impact, the incident momentum flux (per unity ρ) carried by the jet $\pi r_0^2 u_0^2$ is reduced by an amount of order $2\pi r_i \delta u_0 u$, lost in the boundary layer. The step velocity profile at the impactor lip relaxes by viscous smoothing as it leaves the impactor over a short radial distance of order $u_0 h^2/\nu$ towards a uniform (shear-free) profile with velocity u and thickness h, carrying the rest of the momentum $2\pi r h u^2$ and the jet flow

https://doi.org/10.1017/jfm.2013.354 Published online by Cambridge University Press

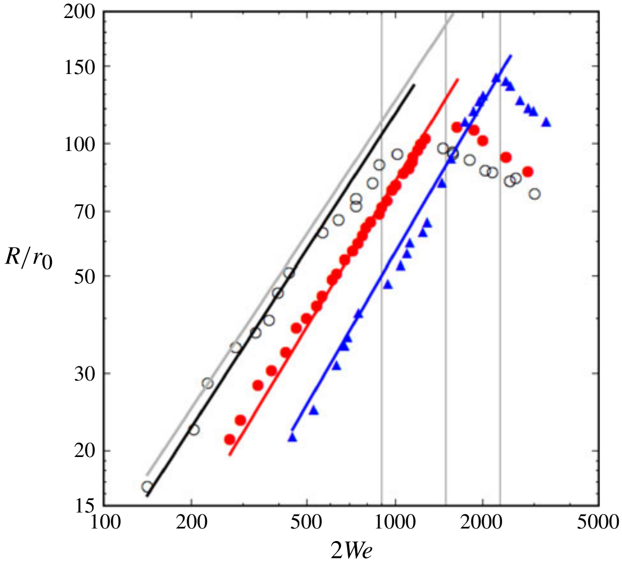

FIGURE 4. (Colour online) Smooth sheet radius for three different viscosities, namely $\nu = \eta/\rho = 10^{-6}$ m^2 s^{-1} (water, open circles, black), $\nu = 60 \times 10^{-3}/1200$ m^2 s^{-1} (filled circles, red online), and $\nu = 320 \times 10^{-3}/1200$ m^2 s^{-1} (filled triangles, blue online). The solid lines are (3.12). The inviscid ($\nu = 0$) reference case for which $R/r_0 = We/4$ is shown as a light grey line: see Villermaux & Clanet (2002) for comparison. The vertical lines indicate the transition Weber numbers to the flapping regime We_c expected from (3.14).

rate $\pi r_0^2 u_0 = 2\pi r h u$. Thus,

$$u = \frac{u_0}{1+\beta} \quad \text{and} \quad h(r) = \frac{r_0^2}{2r}(1+\beta). \tag{3.9}$$

The ratio of the impulse carried by the sheet in a given radial direction (the average over the 2π angular directions is zero for an axisymmetric sheet) to the incident impulse is thus

$$\frac{\text{sheet impulsion}}{\text{incident impulsion}} \sim \frac{u^2 h r_i}{u_0^2 r_0^2} = \frac{1}{1+\beta}, \tag{3.10}$$

indeed smaller than unity. The above relations interpolate between the thin boundary layer limit ($\beta \ll 1$) for which $u \approx u_0(1-\beta)$ and the viscous limit ($\beta \gg 1$) which involves corrections in β^2 (Watson 1964; Clanet & Villermaux 2002).

The radial expansion is halted by capillary confinement, namely when the momentum flux of the sheet equilibrates surface tension forces, or

$$\rho u^2 h(R) = 2\sigma, \tag{3.11}$$

thus providing the sheet radius

$$\frac{R}{r_0} = \frac{We}{4}\frac{1}{1+\beta}. \tag{3.12}$$

Figure 4 shows that (3.12) represents the evolution of the sheet radius R well: as the injection velocity u_0 is varied, both the Weber number and the Reynolds number

https://doi.org/10.1017/jfm.2013.354 Published online by Cambridge University Press

increase, and hence β decreases. The overall dependence of R on We is thus steeper than that known for the inviscid case ($R/r_0 \sim We$), precisely because the relative momentum loss due to viscosity progressively fades away as Re increases.

As anticipated from (3.12), the absolute value of R is smaller, at a given Weber number, for a viscous liquid than for water. This is true for Weber numbers up to the transition to the flapping regime for water (i.e. $2We \approx 10^3$: see Villermaux & Clanet 2002, who were using a Weber number based on d_0), where R saturates and then decays as We increases. However, figure 4 shows that this transition is delayed when the liquid viscosity is larger, and occurs for a higher Weber number. Hence, the maximal radius of a viscous liquid sheet is larger than that of water, a fact that is *a priori* unexpected, but consistent with our understanding of the ingredients ruling the transition to the Squire or flapping regime.

3.3. *Transition to the flapping regime*

A thin liquid sheet expanding in an environment of density ρ_a at rest (air in the present case) is known to interact with it through a Kelvin–Helmholtz type of instability selecting preferentially a sinuous mode (Squire 1953; Huang 1970; Villermaux & Clanet 2002), conferring to the sheet a flapping motion. The instability wavelength λ equilibrates air inertia $\rho_a u^2$ if u is the relative velocity between the in-plane motion of the sheet with ambient air and capillary restoration forces σ/λ. This is primarily an inviscid mechanism. The mode selection in a radially expanding sheet with a thickness profile $h(r) \sim 1/r$ has been discussed in Villermaux & Clanet (2002), including the pre-factors, and we have

$$\lambda = \frac{10\pi\sigma}{\rho_a u^2}. \tag{3.13}$$

This instability is likely to develop and therefore alter the sheet breakup mechanism at its edge (see Bremond *et al.* 2007; Lhuissier & Villermaux 2009, 2012) if at least one wavelength λ can fit within a sheet radius R. The condition $\lambda/R = O(1)$ thus defines a pair $\{We_c, \beta_c\}$ of critical parameters for the transition to occur such that

$$\frac{We_c}{(1+\beta_c)^{3/2}} = \sqrt{\frac{40\pi}{\alpha}}, \tag{3.14}$$

where $\alpha = \rho_a/\rho$. With β given in (3.8), and by plotting the left-hand side of (3.14) divided by $\sqrt{40\pi/\alpha}$ versus We, the criterion above is solved numerically, predicting the transition Weber numbers reported as vertical lines in figure 4, and showing good agreement with the observed ones. Interestingly, the transition Weber number for the most viscous liquid we used ($We_c \approx 2300$) is more than twice as large the one corresponding to water in the same conditions ($We_c \approx 900$), leading to a sheet radius more than 50 % larger, even though viscous losses at the impact region have slowed down the liquid velocity u_0 by 25 % (see (3.9)).

There are, in fact, two concomitant reasons for this delay: the liquid is slowed down, and the sheet is conversely thickened (equation (3.9)). For instance, the sheet thickness at the maximal smooth radial extension is

$$h(R) = \frac{2r_0}{We}(1+\beta)^2. \tag{3.15}$$

It is thus doubly difficult for the weakened shear u (by a factor of $1+\beta$: see (3.9)) to move a thicker – and therefore heavier – sheet (by a factor of $(1+\beta)^2$)

https://doi.org/10.1017/jfm.2013.354 Published online by Cambridge University Press

perpendicular to its plane and trigger an undulatory motion (even if the transit time has been augmented), hence the mandatory recourse to higher Weber numbers for it to be possible, as expressed by (3.14).

4. Fragments

Having reached the border of the sheet, where they are arrested according to (3.11), the fluid particles accumulate in a rim where they dissipate most of their kinetic energy, and are driven at the tip of cusps from which they finally fall by their own weight, forming ligaments that eventually break into stable drops. This is how the spray is formed in a Savart sheet, a scenario qualitatively visible from Savart drawings, and quantified by Clanet & Villermaux (2002).

As figure 1 demonstrates, ligament breakup is delayed with a viscous fluid compared to water. This delay is an intrinsic consequence of the liquid viscosity which slows down the capillary instability of jets (Eggers & Villermaux 2008), and has an important consequence for the shape of the resulting distribution $P(d)$ of the drop sizes d.

4.1. *Repartition of drops*

When a liquid protrusion, having accumulated in the rim, is heavy enough to overcome the capillary retraction of the sheet to which it is attached, it falls by gravity. However, that big drop remains transiently attached to the sheet by a ligament. As the big drop falls, the ligament stretches, and detaches by capillary breakup from both the sheet and the big drop. After detachment, the ligament finally recoils into a smaller satellite drop. This scenario, where capillary instabilities follow each other sequentially, was already visible in Plateau's experiments with olive oil (Plateau 1873), and has since then been identified in related contexts involving viscous fluids (Tjahjadi, Stone & Ottino 1992; Brenner, Shi & Nagel 1994; Wong *et al.* 2004). It is illustrated in figure 6. It causes notorious difficulties in inkjet printing in particular (Basaran, Gao & Bhat 2013). With water, the capillary breakup is so fast that the phenomenon is virtually absent, unless altered by *ad hoc* perturbations (Lafrance & Ritter 1977).

The direct consequence of the scenario depicted above is the bimodal character of the drop size distribution in the spray, which present two (broad) peaks, as seen in figure 5. The peak characteristic of the biggest drops in the distribution has an average $\langle d\rangle$ which slowly shifts towards smaller sizes d as We increases, while the peak corresponding to the smallest drops follows the same trend, with an average diameter $\langle d_s\rangle$ such that

$$\frac{\langle d_s\rangle}{\langle d\rangle}=\gamma, \tag{4.1}$$

with $\gamma^{-1}\approx 3$–5 approximately.

The maximal probability levels of both peaks are of the same order, with no systematic trend dependence on We. If a difference exists between the probability levels of the two peaks, it is always at the advantage of the small drops, as seen in figure 5. The peaks corresponding to the biggest drops in the distribution $P_>(d)$ is invariant with We when the drop sizes are rescaled by $\langle d\rangle$, and is well approximated by a Gamma distribution characteristic of ligament-mediated drop formation (Villermaux 2007):

$$P_>(x=d/\langle d\rangle)=\frac{n^n}{\Gamma(n)}x^{n-1}\mathrm{e}^{-nx} \tag{4.2}$$

https://doi.org/10.1017/jfm.2013.354 Published online by Cambridge University Press

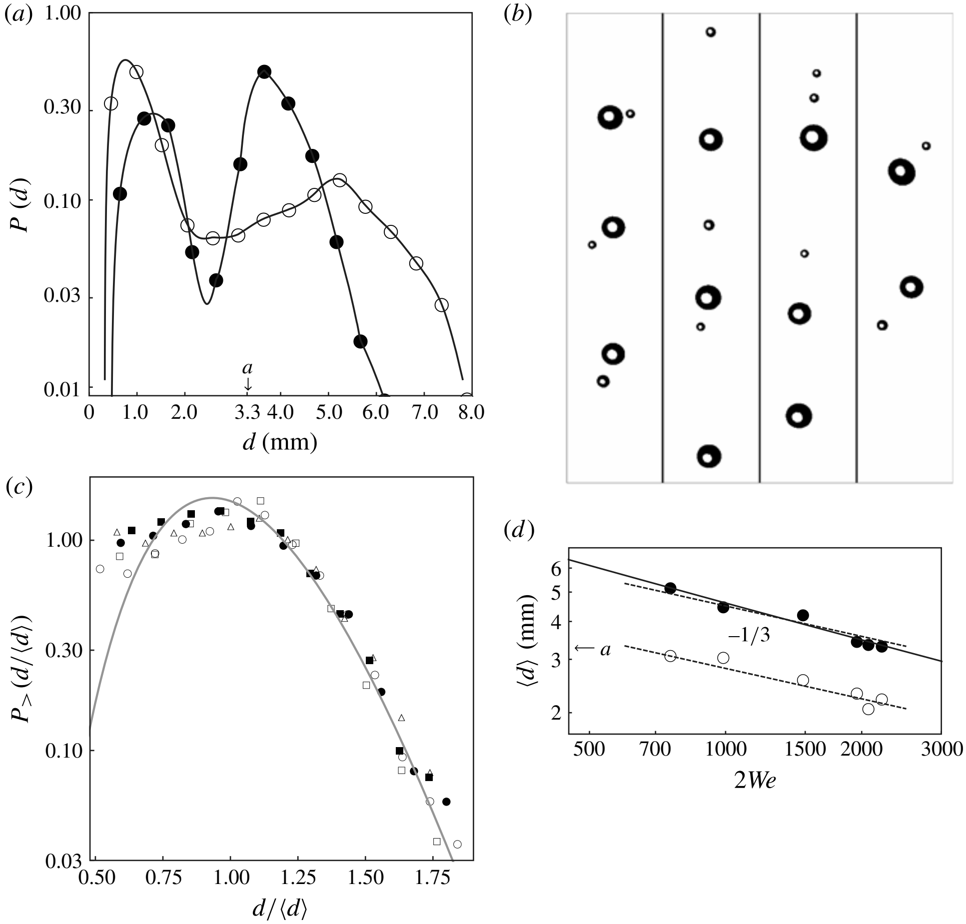

FIGURE 5. Drop size distributions and average diameters obtained for $\eta = 320 \times 10^{-3}$ Pa s. (*a*) Examples of drop size distributions with a double peak: ○, $We = 755$; ●, $We = 988$. (*b*) A series of typical snapshots in the spray illustrating the alternation of big and small drops, in even proportions: $We = 988$. (*c*) The large excursion peak of the distribution $P_>(d)$ rescaled by its average diameter $\langle d\rangle$ for various Weber numbers ranging from 755 to 2213. The solid line is a Gamma distribution of order 15. (*d*) The large excursion peak average diameter $\langle d\rangle$ (●), and the total average of the distribution $3\langle d\rangle/5$ as a function of We_a (○). The solid line is (4.5). The dotted lines are the dominant $We_a^{-1/3}$ dependence.

of order $n = 15$, as seen in figure 5. This fact is reminiscent of an identical observation made by Bremond *et al.* (2007) for water Savart sheets, though with a lower Gamma order ($n = 5$), indicating a broader distribution around the mean in that case.

The size of the big droplets simply results from a static (and thus independent of viscosity) force balance similar to Tate's law (Bouasse 1924), where the weight of the detaching protrusion at the sheet rim equilibrates capillary retraction (Clanet & Villermaux 2002):

$$\rho g \Omega_\star \sim \sigma h(R), \tag{4.3}$$

with $h(R)$ given in (3.15), and where $\Omega_\star$ is the critical volume of the protrusion. Obviously

$$\Omega_\star \approx \langle d^3\rangle + \langle d_s^3\rangle \tag{4.4}$$

https://doi.org/10.1017/jfm.2013.354 Published online by Cambridge University Press

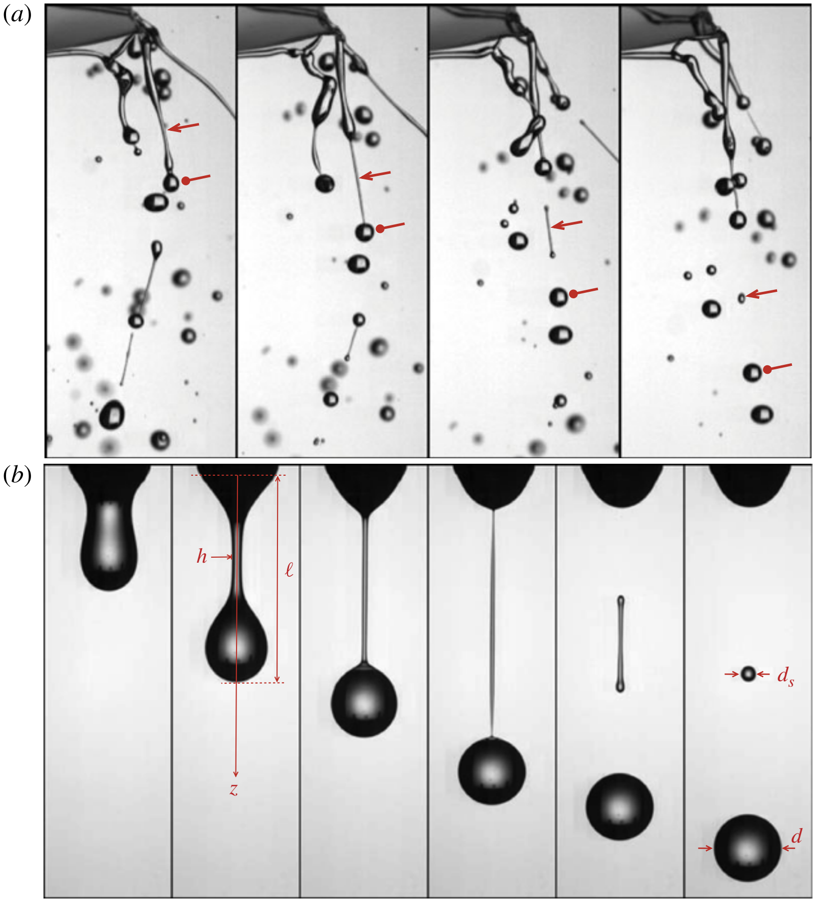

FIGURE 6. (Colour online) Ligaments and the mechanism for the bimodal drop size distribution formation, for $\eta = 320 \times 10^{-3}$ Pa s. (*a*) Consecutive views showing the detachment of a big drop followed by the recoil of a ligament into a smaller satellite. (*b*) The model experiment of a dripping tap (of diameter 7 mm) for consecutive times $t = 0, 55, 67, 79, 84, 90$ ms.

since the peaks of the small and large drops have identical relative probabilities in $P(d)$. At this level of description, substituting $\langle d\rangle^3$ for $\langle d^3\rangle$, and since $\langle d_s\rangle/\langle d\rangle = \gamma$ with $\gamma \ll 1$, we have $\Omega_\star \approx \langle d\rangle^3$, leading to, from (4.3) and (3.15),

$$\frac{\langle d\rangle}{a} = \left(\frac{(1+\beta)^2}{We_a}\right)^{1/3} \quad \text{where } We_a = \frac{\rho u_0^2 a}{\sigma}, \tag{4.5}$$

with a the capillary length scale:

$$a = \sqrt{\frac{2\sigma}{\rho g}} \approx 3.3 \text{ mm}. \tag{4.6}$$

The total mean drop size of the distribution is expected to be

$$\frac{\langle d\rangle + \langle d_s\rangle}{2} \approx \frac{\gamma+1}{2}\langle d\rangle \tag{4.7}$$

https://doi.org/10.1017/jfm.2013.354 Published online by Cambridge University Press

which fits the measured mean well with $\gamma = 1/5$ (this value is justified from elementary fluid mechanics in § 5), as seen in figure 5.

Relation (4.5) represents well the measured mean drop sizes of the large excursion peak, exhibiting a slight deviation from the $We_a^{-1/3}$ dominant behaviour because of the Reynolds number dependence of the sheet thickness via the parameter β. The mean drop size $\langle d\rangle$ is essentially given by a, and depends on the sheet injection diameter d_0 via the viscous corrections β only. This is consistent in trend and in absolute value with Clanet & Villermaux (2002), who found with water ($\beta \rightarrow 0$) that the mean drop size was independent of the injection diameters provided that they were larger than a.

5. Bimodality and the origin of small drops

Inspired by the ligament detachment and breakup phenomena observed at the rim of the sheet (figures 1 and 6), we study a simplified version of the process using an analogous experiment intended to explain the origin of the two distinct peaks in the drop size distribution, the ratio of their respective characteristic diameters, and of their relative occurrence in the spray: the small drops are typically as frequent as the big ones (one small drop for one big drop), and are $\gamma^{-1} = 5$ times smaller.

The explanation uses an analogous experiment, a simple dripping tap (i.e. a faucet) with the most viscous solution ($\eta = 320 \times 10^{-3}$ Pa s). The tap's diameter (7 mm) is larger than the capillary length a, which therefore remains the only relevant length scale setting the drop size (Rayleigh 1899), as in the real sheet case if one disregards the weak Weber correction in (4.5). The drop hanging at the tap's exit is slowly fed (at flow rate 1.03×10^{-7} m^3 s^{-1} corresponding to one detaching drop per second) and eventually detaches when it is heavy enough. In doing so, it stretches a ligament attached to the tap's exit. The elongated ligament finally breaks up at its extremities, one at the tap's exit and the other at the falling drop: see figure 6. In contrast to the case for water, the detachment takes a longer time period, and does so on a viscous-dominated time scale. When the ligament has detached from both ends, it recoils to form a unique drop, accumulating all the liquid initially contained in the ligament. This is because the recoil time is shorter than the capillary destabilization time of the ligament. Thus, every time a big drop detaches, its companion ligament produces a satellite drop. This explains why the small drops are typically as frequent as the big ones in the spray. The analysis of this scenario further provides the ratio of satellite to main drop diameters.

5.1. *Energetics of a caricatured pendant drop*

We describe below the early time dynamics of the detachment of a drop, whose geometry is suitably caricatured for the analysis to be simple, attached to a ceiling as in figure 7.

The energy of a liquid volume $\varOmega$ caricatured as a cylinder of base radius h and height ℓ, hanging by gravity from a ceiling (or a tap, as in figure 6), is

$$E = -\int_0^{\ell} \rho g \pi h^2 z \,\mathrm{d}z + \sigma(\pi h^2 + 2\pi h \ell), \tag{5.1}$$

$$\varOmega = \pi h^2 \ell. \tag{5.2}$$

Recalling that the capillary length scale is $a = \sqrt{2\sigma/\rho g}$ and setting

$$x = \frac{\ell}{a}, \tag{5.3}$$

https://doi.org/10.1017/jfm.2013.354 Published online by Cambridge University Press

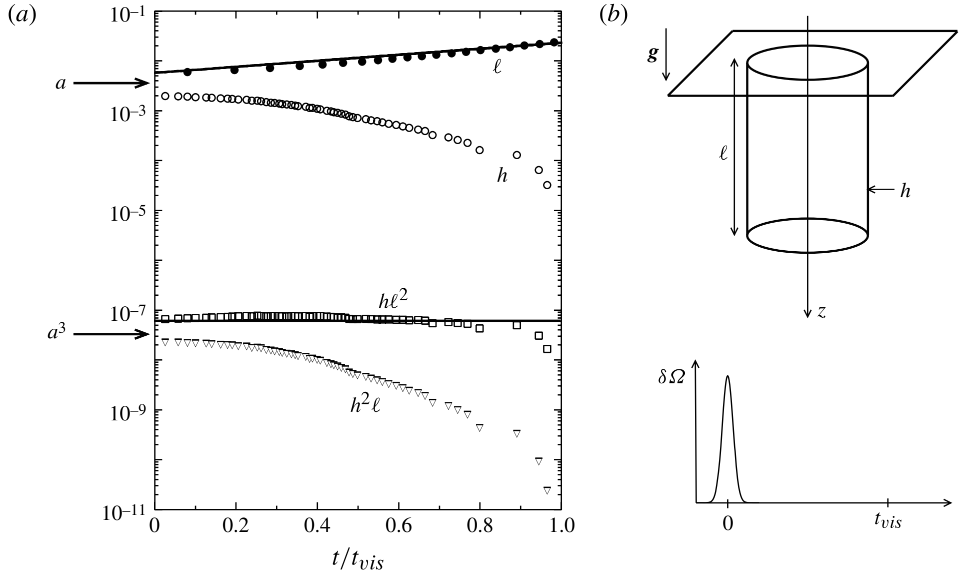

FIGURE 7. (*a*) Evolution of the length ℓ, radius h and volume $h^2\ell$ of the ligament in figure 6, almost independent of time in units of the viscous destabilization time $t_{vis} \approx 0.085$ s. Also shown is the quantity $h\ell^2$, as a function of time. Lengths are in metres and volumes in cubic metres ($a = 0.0033$ m and $a^3 = 3.6 \times 10^{-8}$ m^3 are shown for reference). (*b*) Sketch of the cylindrical drop geometry, and the velocity of the volumetric pulse $\delta\Omega$.

$$\epsilon = \sqrt{\frac{\pi a^3}{\Omega}}, \tag{5.4}$$

we have

$$\frac{E}{\rho g \Omega a} = -\frac{x}{2} + \frac{1}{2x} + \epsilon\sqrt{x}. \tag{5.5}$$

If the liquid volume elongates in the gravity field, it lowers its potential energy, while the corresponding deformation is made at the expense of an increase in its surface energy. When the liquid volume is small enough (i.e. in the limit of large ϵ), the total energy E has a minimum $\mathrm{d}E/\mathrm{d}x = 0$, and the drop hangs stably with a length $x = \ell/a$ as a function of ϵ. As the volume increases (i.e. ϵ decreases), the equilibrium is lost, and E is a monotonically decreasing function of x. This happens first for $\mathrm{d}E/\mathrm{d}x = 0$ and $\mathrm{d}^2E/\mathrm{d}x^2 = 0$, giving the critical condition

$$x_\star = \sqrt{3}, \tag{5.6}$$

$$\epsilon_\star = \frac{4}{3^{3/4}}, \tag{5.7}$$

simply expressing that the dimensions of the critical drop are given by the capillary length scale a, a well-known fact (Rayleigh 1899; Bouasse 1924).

We now examine the dynamics of the destabilization of the above equilibrium when the liquid volume is slightly increased by an amount $\delta\Omega$ from the critical volume $\Omega_\star$ (correspondingly, $\delta\epsilon/\epsilon_\star = -(\delta\Omega/\Omega_\star)/2$). Neglecting viscous dissipation close to

https://doi.org/10.1017/jfm.2013.354 Published online by Cambridge University Press

equilibrium, the rate of change of the liquid volume momentum is

$$\frac{\mathrm{d}}{\mathrm{d}t}\int_0^{\ell} \rho\pi h^2 v(z,t)\,\mathrm{d}z = -\frac{\mathrm{d}E}{\mathrm{d}\ell} \tag{5.8}$$

$$= -a\frac{\mathrm{d}E}{\mathrm{d}x}. \tag{5.9}$$

The axial velocity $v(z,t)$ in the liquid volume is such that, by incompressibility $\partial_t h^2 + \partial_z(vh^2) = 0$, and since h only depends on time in this cylindrical caricature, we have ($\dot{\ell} = \mathrm{d}\ell/\mathrm{d}t$)

$$v(z,t) = \frac{\dot{\ell}}{\ell} z. \tag{5.10}$$

Owing to (5.9), the reduced length $x = x_\star + \delta x$ is augmented, above the critical condition, by an amount δx whose rate of increase in time is prescribed by the rate at which the energy E decays when x is increased, that is, by the slope $\mathrm{d}E/\mathrm{d}x$ in $x = x_\star$. When time is made dimensionless by $\sqrt{a/g}$, at the critical point we have $\ddot{\delta x} = -\delta\epsilon/\sqrt{x_\star}$, or

$$\ddot{\delta x} = \frac{2}{3}\frac{\delta\Omega}{\Omega_\star}. \tag{5.11}$$

If the volume $\delta\Omega$ were initially added in the critical cylinder, and remained in it for $t > 0$, then the early time motion of its height would be parabolic in time, with an apparent gravity depending on $\delta\Omega$.

5.2. *More realistic geometry and dynamics*

This is precisely the point at which our cylindrical caricature must be corrected. A critical hanging drop is not exactly a cylinder (see Boucher & Evans 1975 and historical references therein), and a detaching drop certainly not either. Most of the liquid volume is collected in a close-to-spherical falling volume, which remains connected to the ceiling, or the tap nozzle, via an elongating ligament whose shape is, in turn, quite close to a cylinder (figure 6). The internal pressure in the cylindrical ligament is the Laplace pressure σ/h, and when it is connected to a sphere with radius much larger than h, is likely to 'empty' into it. The volume $\delta\Omega$ is thus unlikely to remain constant in time, since the more the ligament elongates the stronger the Laplace pressure will be, enhancing the drain of the ligament. The drain will, however, stop at some point because, as we will see, the elongated ligament destabilizes and breaks up at its extremities. Overall, the volume $\delta\Omega$ therefore first increases and then decreases, so the net incorporated volume is close to zero. (In fact it is not exactly zero. It is known that the weight of a drop detaching from a tap depends on the flow rate feeding it, even in the limit of very slow flow rates: Harkins & Brown 1919. Here we disregard this correction.) We postulate that this volumetric pulse occurs within a time scale that is short compared with the destabilization time of the ligament, an assumption proved to be correct later. We then have

$$\delta\Omega = \omega\delta(t), \tag{5.12}$$

where $\delta(t)$ is a Dirac delta and time t is in units of $\sqrt{a/g}$ so that ω is a volume, *a priori* smaller that the critical volume of the drop $\Omega_\star$, and independent of the flow

https://doi.org/10.1017/jfm.2013.354 Published online by Cambridge University Press

rate feeding the drop in the limit of small flow rates. Since

$$x \approx x_\star \exp\left(\frac{\delta x}{x_\star}\right) \tag{5.13}$$

$$= x_\star \exp\left(\frac{2}{3x_\star}\int_0^t \mathrm{d}t_1 \int_0^{t_1} \frac{\delta \Omega}{\Omega_\star}\right) \tag{5.14}$$

we have finally, with (5.12) and with the dimensional time restored,

$$x = x_\star \exp\left(\frac{2\omega}{3\Omega_\star x_\star}\frac{t}{\sqrt{a/g}}\right). \tag{5.15}$$

Comparison with the direct measurements of both h and $\ell = a\,x$, reported in figure 7, shows that ℓ indeed grows exponentially from a value not far from $a\sqrt{3} \approx 0.0057$ m. These measurements are compatible with

$$\ell = a\sqrt{3}\exp\left(0.3\frac{t}{\sqrt{a/g}}\right), \tag{5.16}$$

suggesting that $\omega \approx 0.8\Omega_\star$.

The motion of the axial velocity $v(z, t)$ in the ligament is governed by

$$\partial_t v + v\partial_z v = -\frac{1}{\rho}\partial_z p - \frac{3\nu}{h^2}\partial_z(h^2\partial_z v), \tag{5.17}$$

which identically cancels the viscous Trouton term in the cylindrical approximation where $v(z, t)$ is given by (5.10). Integrating (5.17) between $z \approx 0$, where the pressure is $p(0, t) \approx \sigma/h$ (somewhere close to the base of the ligament), and $z = \ell$, where $p(\ell, t) \approx 0$ (in the big hanging drop), we get

$$h\ell\ddot{\ell} = \frac{2\sigma}{\rho} \tag{5.18}$$

or, since ℓ given in (5.16) is exponential in time,

$$h\ell^2 \approx a^3. \tag{5.19}$$

Figure 7 shows that $h\ell^2$ is indeed roughly constant during the ligament elongation, unlike the ligament volume which, scaling like $h^2\ell$, decreases in time, consistent with our scenario where the ligament empties into the big drop to which it is attached as it elongates.

The above analysis suits the early time dynamics, where all the components of the energy E in (5.5) are balanced, or nearly so. Later, when most of the mass has concentrated in the heavy hanging drop, whose weight ($\sim\rho g a^3$) rapidly overcomes the capillary ($\sim\sigma h$) and viscous ($\sim\eta h^2\dot{\ell}/\ell$) stresses from the thinning ligament attached to it, the dynamics of the hanging drop is of course that of free fall (i.e. $\ell \sim g t^2/2$). However, as will be seen, this ultimate regime is never reached, ligament breakup having occurred earlier.

5.3. *Breakup and satellite drop*

Stretching inhibits capillary destabilization (Tomotika 1936; Stone 1994). However, the time taken for the extremities of the ligament to detach from the main drop, and from the tap's exit, is independent of the rate at which the ligament is stretched, and is

https://doi.org/10.1017/jfm.2013.354 Published online by Cambridge University Press

solely prescribed by the relevant instability time scale t_{cap} if only capillarity and liquid inertia are at play, or t_{vis} if viscous slowing is dominant. Here

$$t_{cap} \approx 3\sqrt{\frac{\rho h_\star^3}{\sigma}} \quad \text{and} \quad t_{vis} \approx 6\,\frac{\eta h_\star}{\sigma}, \tag{5.20}$$

keeping the pre-factors of Eggers & Villermaux (2008), based on the initial transverse size of the ligament $h_\star = (3\sqrt{3}/4)\,a \approx 1.3a$. Indeed, the stretching vanishes at the extremities (on an axial distance of the order of $h_\star$), which are pinned at the main drop surface and at the tap's exit (this is also true when the ligament is attached to the sheet). These regions at the extremities thus evolve on their own, basically insensitive to the rest of the (stretched) ligament (Henderson *et al.* 2000; Villermaux 2012).

The ratio of these two time scales above defines the relevant capillary (or Ohnesorge) number for deciding which characteristic time is the longest, and hence, if viscosity impacts the capillary destabilization of the ligament extremities,

$$\frac{t_{vis}}{t_{cap}} = 2\frac{\eta}{\sqrt{\rho h_\star \sigma}} \tag{5.21}$$

$$= \sqrt{2}Ca, \tag{5.22}$$

where

$$Ca = \frac{\eta\sqrt{ga}}{\sigma} \approx 0.8. \tag{5.23}$$

Thus $\sqrt{2}Ca$ is slightly above unity, suggesting that t_{vis} is the relevant instability time scale, and indeed the observations in figure 6 show that breakup has occurred precisely at t_{vis}. As long as it is stretched, the rest of the ligament does not develop instabilities since $(\dot{\ell}/\ell)\,t_{vis} > 1$. From (5.16) and (5.20), the length of the ligament at breakup is

$$\ell_s = a\sqrt{3}\exp(0.3 \times 6Ca). \tag{5.24}$$

Once detached the ligament is no longer stretched, and is thus likely to destabilize by capillarity. The relevant time scale is again t_{vis}, this time based on the value of h at detachment, deduced from the invariance of $h\ell^2$ during the elongation process (figure 7):

$$h_s = a^3/\ell_s^2. \tag{5.25}$$

That destabilization competes with the spontaneous recoil of the ligament from its extremities, receding at velocity

$$v_{rec} = \sqrt{\frac{\sigma}{\rho h_s}}, \tag{5.26}$$

identical to that of a the plane edge of a liquid sheet (Culick 1960), and insensitive to viscosity (Savva & Bush 2009). The ratio of the recoil time $\ell_s/(2v_{rec})$ to the capillary instability time of the ligament $6\eta h_s/\sigma$ is precisely given by Ca in (5.23), and is therefore slightly below unity in the present case, consistent with the observed fact that all the volume constituting the ligament is included in a single satellite drop (see also Notz & Basaran 2004; Eggers & Fontelos 2005; Castrejon-Pita, Castrejon-Pita & Hutchings 2012; Hoath, Jung & Hutchings 2013). Its volume is such that (we assimilate $\ell - a$ with ℓ at detachment)

$$\Omega_s = \pi h_s^2 \ell_s, \tag{5.27}$$

https://doi.org/10.1017/jfm.2013.354 Published online by Cambridge University Press

while the volume of the main drop is of order

$$\Omega_\star = \pi h_\star^2 \ell_\star \approx a^3. \tag{5.28}$$

The volume of the ligament at breakup is indeed a small fraction of that of the main drop,

$$\frac{\Omega_s}{\Omega_\star} \approx \exp(-6Ca) \approx 0.0082, \tag{5.29}$$

giving

$$\frac{d_s}{a} \approx \exp(-2Ca) \approx 0.20, \tag{5.30}$$

where $d_s = a(\Omega_s/\Omega_\star)^{1/3}$ denotes the secondary stable droplet diameter having collected the ligament volume, consistent with the observations reported in both our model dripping experiment (figure 6), and in the spray formed from the Savart sheet, at the same viscosity ($\gamma \approx 1/5$ in (4.1)). This simple model explains both the occurrence of one secondary smaller drop per main drop, the order of magnitude of the main drop size, given by a (the weak Weber correction has been explained in § 4.1), and the ratio of the small to main sizes.

6. Conclusions and further remarks

180 years after his seminal publications in the *Annales de Chimie*, we have supplemented one aspect of Savart's observations with the case where viscosity matters. When a radially expanding sheet is formed by the impact of a viscous liquid jet on a solid disk, two new observations concerning the viscous limit are made.

For a given jet radius and impacting velocity, the viscous sheet radius can be larger compared to water because the smooth–flapping transition is delayed as the jet velocity is increased. There are two concomitant reasons for this delay: because a boundary layer forms at the surface of the disk, the liquid is slowed down as it expands, and the sheet is conversely thickened. It is thus doubly difficult for the weakened shear with the ambient air to move a thicker (and therefore heavier) sheet perpendicular to its plane and trigger an undulatory motion which would destroy the sheet within one oscillation.

Viscosity not only delays shear instabilities (indirectly in the present case) but also delays capillary breakup, providing the source of the second surprising observation: the final drop size distribution is bimodal, with a substantial fraction of the drops having a smaller, well-defined diameter. These originate in the recoil of ligaments left behind the main drops detaching from the sheet rim. The ligaments stretch as long as they are destabilized by capillarity, on a time scale increased by viscosity. The ratio of the satellite to the main drop diameter only depends on the capillary number Ca via (5.29). The main drop size is not appreciably affected by viscosity, since it results from a static equilibrium between weight and capillary retraction, as seen from (4.5) and figure 5. Thus, for a fixed viscosity, the relative distance between the two peaks in the global drop size distribution $P(d)$ is independent of the injection Weber number We. However, increasing the liquid viscosity (and thus Ca) delays ligament breakup, thus making the ligament thinner at breakup, hence producing smaller satellite drops relative to the main drop. Smaller objects are thus paradoxically produced through viscous slowing.

https://doi.org/10.1017/jfm.2013.354 Published online by Cambridge University Press

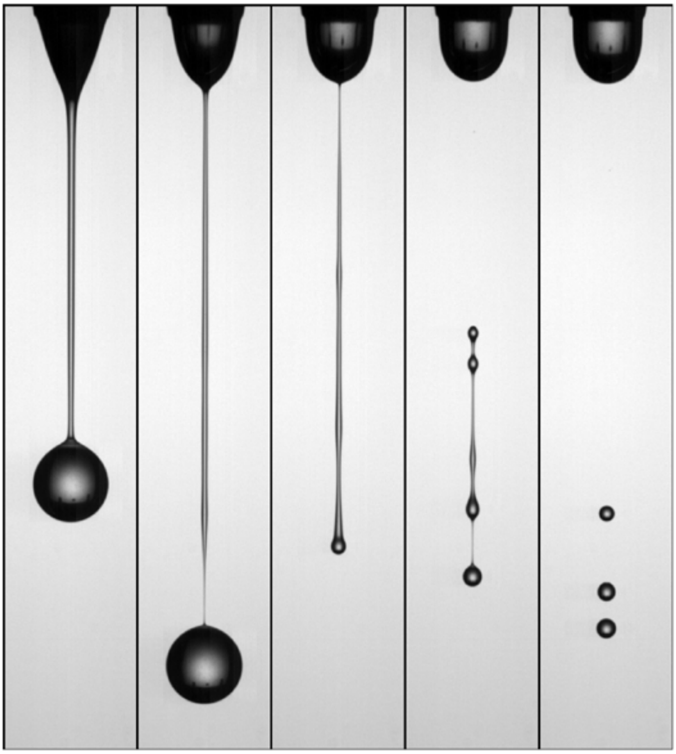

FIGURE 8. Consecutive views showing the detachment of a drop from a tap 5 mm in diameter (injection flow rate 2.8×10^{-7} m^3 s^{-1}), followed by partial recoil and fragmentation of a ligament into three smaller satellites. The snapshots are separated by 11 ms; $\eta = 320 \times 10^{-3}$ Pa s.

Note that the criterion for having only one satellite drop from a recoiling ligament is that its capillary destabilization time is larger than the recoil time. In the opposite case, the ligament breaks faster than it recoils (into a number of the order of ℓ_s/h_s drops in the extremely slow recoil and fast destabilization limit). Since the two times compare to each other in our tap experiment, even a minute change in the injection protocol alters the number of satellites. Figure 8 shows how using a slightly smaller injection diameter with a somewhat larger injection flow rate produces a longer ligament, which fragments into three rather than one unique satellite. Such variations occur naturally in the real sheet case, explaining the tendency to have proportionally more small drops than big drops – up to a factor of 3, to be precise, as seen by comparing the probability levels of the two peaks for $We = 755$ in figure 5. This observation is consistent with our understanding of the mechanism producing the bimodality of the drop size distribution with viscous fluids, and also underlines the limits of our simple analogous experiment, and the theory we have made of it.

Finally, although the mechanism described here produces ligaments thinning approximately exponentially in time, it should not be confused with the similar phenomenology involved in viscoelastic fluids (Entov & Hinch 1997; Oliveira & McKinley 2005; Gier & Wagner 2012). Maltodextrin is a Newtonian liquid, which does not resist stretching with internal elastic stresses. The dynamics of the ligament elongation here results from the slow deformation of the energy landscape balancing

https://doi.org/10.1017/jfm.2013.354 Published online by Cambridge University Press

gravity with capillarity, and not from an equilibrium between relaxing elastic stresses and capillarity. Extending the Savart sheet problem to viscoelastic fluids, for which bimodal drop size distributions have been observed in jet breakup (Christianti & Walker 2000), would be another endeavour.

REFERENCES

Basaran, O. A., Gao, H. & Bhat, P. P. 2013 Nonstandard inkjets. *Annu. Rev. Fluid Mech.* **45**, 85–113.

Bouasse, H. 1924 *Capillarité*. Delagrave.

Boucher, E. A. & Evans, J. B. 1975 Pendent drop profiles and related capillary phenomena. *Proc. R. Soc. Lond.* A **346**, 349–374.

Bremond, N., Clanet, C. & Villermaux, E. 2007 Atomization of undulated liquid sheets. *J. Fluid Mech.* **585**, 421–456.

Bremond, N. & Villermaux, E. 2006 Atomization by jet impact. *J. Fluid Mech.* **549**, 273–306.

Brenner, M. P., Shi, X. D. & Nagel, S. R. 1994 Iterated instabilities during droplet fission. *Phys. Rev. Lett.* **73** (25), 3391–3394.

Castrejon-Pita, A. A., Castrejon-Pita, J. R. & Hutchings, I. M. 2012 Breakup of liquid ligaments. *Phys. Rev. Lett.* **108**, 074506.

Christianti, Y. & Walker, L. M. 2000 Surface tension driven jet break up of strain-hardening polymer solutions. *J. Non-Newtonian Fluid Mech.* **100**, 9–26.

Clanet, C. & Villermaux, E. 2002 Life of a smooth liquid sheet. *J. Fluid Mech.* **462**, 307–340.

Culick, F. E. C. 1960 Comments on a ruptured soap film. *J. Appl. Phys.* **31**, 1128–1129.

Dokic, P., Jakovljevic, J. & Dokic-Baucal, L. 1998 Molecular characteristics of maltodextrins and rheological behaviour of diluted and concentrated solutions. *Colloids Surf.* A **141**, 435–440.

Eggers, J. & Fontelos, M. A. 2005 Isolated inertialess drops cannot break up. *J. Fluid Mech.* **530**, 177–180.

Eggers, J. & Villermaux, E. 2008 Physics of liquid jets. *Rep. Prog. Phys.* **71**, 036601.

Entov, V. M. & Hinch, E. J. 1997 Effect of a spectrum of relaxation times on the capillary thinning of a filament of elastic liquid. *J. Non-Newtonian Fluid Mech.* **72**, 31–53.

Gier, S. & Wagner, C. 2012 Visualization of the flow profile inside a thinning filament during capillary breakup of a polymer solution via particle image velocimetry and particle tracking velocimetry. *Phys. Fluids* **24**, 053102.

Harkins, W. D. & Brown, F. E. 1919 The determination of surface tension (free surface energy), and the weight of falling drops: the surface tension of water and benzene by the capillary height method. *J. Am. Chem. Soc.* **41**, 499–524.

Henderson, D., Segur, H., Smolka, L. B. & Wadati, M. 2000 The motion of a falling liquid filament. *Phys. Fluids* **12** (3), 550–565.

Hoath, S. D., Jung, S. & Hutchings, I. M. 2013 A simple criterion for filament break-up in drop-on-demand inkjet printing. *Phys. Fluids* **25**, 021701.

Howell, P. D., Scheid, B. & Stone, H. A. 2010 Newtonian pizza: spinning a viscous sheet. *J. Fluid Mech.* **659**, 1–23.

Huang, J. C. P. 1970 The break-up of axisymmetric liquid sheets. *J. Fluid Mech.* **43**, 305–319.

Lafrance, P. & Ritter, R. C. 1977 Capillary breakup of a liquid jet with a random initial perturbation. *J. Appl. Mech.* 385–388.

Landau, L. & Lifshitz, E. 1987 *Fluid Mechanics*. Pergamon.

Lefebvre, A. H. 1989 *Atomization and Sprays*. Hemisphere.

Lhuissier, H. & Villermaux, E. 2009 Soap films burst like flapping flags. *Phys. Rev. Lett.* **103**, 054501–(4).

Lhuissier, H. & Villermaux, E. 2012 Crumpled water bells. *J. Fluid Mech.* **693**, 508–540.

Mastin, L. G. 2007 Generation of fine hydromagmatic ash by growth and disintegration of glassy rinds. *J. Geophys. Res.* **112**, B02203.

https://doi.org/10.1017/jfm.2013.354 Published online by Cambridge University Press

Notz, P. K. & Basaran, O. A. 2004 Dynamics and breakup of a contracting liquid filament. *J. Fluid Mech.* **512**, 223–256.

Oliveira, M. & McKinley, G. 2005 Iterated stretching and multiple beads-on-a-string phenomena in dilute solutions of high extensible flexible polymers. *Phys. Fluids* **17**, 071704.

Plateau, J. 1873 *Statique Expérimentale et Théorique des Liquides Soumis aux Seules Forces Moléculaires*. Gauthiers-Villars.

Rayleigh, Lord 1899 Investigations in capillarity. *Phil. Mag.* **48**, 321–337.

Savart, F. 1833*a* Mémoire sur le choc d'une veine liquide lancée sur un plan circulaire. *Ann. Chim.* **54**, 56–87.

Savart, F. 1833*b* Suite du mémoire sur le choc d'une veine liquide lancée sur un plan circulaire. *Ann. Chim.* **54**, 113–145.

Savva, N. & Bush, J. W. M. 2009 Viscous sheet retraction. *J. Fluid Mech.* **626**, 211–240.

Schlichting, H. 1987 *Boundary Layer Theory*, 7th edn. McGraw-Hill.

Semenova, M. G., Belyakova, L. E., Antipova, A. S., Polikarpov, Y. N., Klouda, L., Markovic, A. & Il'in, M. M. 2003 Effect of maltodextrins on the surface activity of small-molecule surfactants. *Colloids Surf.* B **31**, 47–54.

Squire, H. B. 1953 Investigation of the stability of a moving liquid film. *British J. Appl. Phys.* **4**, 167–169.

Stone, H. A. 1994 Dynamics of drop deformation and breakup in viscous fluids. *Annu. Rev. Fluid Mech.* **26**, 65–102.

Taylor, G. I. 1959*a* The dynamics of thin sheets of fluid. Part 2. Waves on fluid sheets. *Proc. R. Soc. Lond.* A **253**, 296–312.

Taylor, G. I. 1959*b* The dynamics of thin sheets of fluid. Part 3. Disintegration of fluid sheets. *Proc. R. Soc. Lond.* A **253**, 313–321.

Tjahjadi, M., Stone, H. A. & Ottino, J. M. 1992 Satellite and subsatellite formation in capillary breakup. *J. Fluid Mech.* **243**, 297–317.

Tomotika, S. 1936 Breaking up of a drop of viscous liquid immersed in another fluid which is extending at uniform rate. *Proc. R. Soc Lond.* A **153**, 302–318.

Villermaux, E. 2007 Fragmentation. *Annu. Rev. Fluid Mech.* **39**, 419–446.

Villermaux, E. 2012 The formation of filamentary structures from molten silicates: Pele's hair, angel hair, and blown clinker. *C. R. Mécanique* **340**, 555–564.

Villermaux, E. & Clanet, C. 2002 Life of a flapping liquid sheet. *J. Fluid Mech.* **462**, 341–363.

Watson, E. J. 1964 The radial spread of a liquid jet over a horizontal plane. *J. Fluid Mech.* **20**, 481–499.

Wong, D. C. Y., Simmons, M. J. H., Decent, S. P., Parau, E. I. & King, A. C. 2004 Break-up dynamics and drop size distributions created from spiralling liquid jets. *Intl J. Multiphase Flow* **30**, 499–520.

Yule, A. J. & Dunkey, J. J. 1994 *Atomization of Melts*. Clarendon.

https://doi.org/10.1017/jfm.2013.354 Published online by Cambridge University Press